Journal of Applied Physics

AIP Publishing

Growth-Microstructure-Thermal Property Relations in AlN Thin Films

Yiwen Song,[1] Chi Zhang,[2] James Spencer Lundh,[1] Hsien-Lien Huang,[3] Yue Zheng,[4] Yingying Zhang,[2] Mingyo Park,[4] Timothy Mirabito,[5] Rossiny Beaucejour,[6] Chris Chae,[3] Nathaniel Mcllwaine,[3] Giovanni Esteves,[7] Thomas E. Beechem,[8] Craig Moe,[9] Rytis Dargis,[10] Jeremy Jones,[11] Jacob H. Leach,[12] Robert M. Lavelle,[13] David W. Snyder,[13] Jon-Paul Maria,[5] Roy H. Olsson III,[6] Joan M. Redwing,[5] Azadeh Ansari,[4] Jinwoo Hwang,[3] Xiaojia Wang,[2] Brian M. Foley,[1] Susan E. Trolier-McKinstry,[5] and Sukwon Choi[1,a)]

[1]*Department of Mechanical Engineering, The Pennsylvania State University, University Park, PA 16802, USA*

[2]*Department of Mechanical Engineering, University of Minnesota, Minneapolis, MN 55455, USA*

[3]*Department of Materials Science and Engineering, The Ohio State University, Columbus, Ohio 43210, United States*

[4]*School of Electrical and Computer Engineering, Georgia Institute of Technology, Atlanta, GA*

[5]*Department of Materials Science and Engineering, The Pennsylvania State University, University Park, PA 16802, USA*

[6]*Department of Electrical and Systems Engineering, University of Pennsylvania, Philadelphia, PA 19104, USA*

[7]*Microsystems Engineering, Science and Applications (MESA), Sandia National Laboratories, Albuquerque, NM 87123, USA*

[8]*School of Mechanical Engineering and Birck Nanotechnology Center, Purdue University, West Lafayette, Indiana 47904, USA*

[9]*Akoustis, Inc., Canandaigua, NY 14424, USA*

[10]*IQE Plc, Greensboro, NC 27407, USA*

[11]*Nitride Global Inc., Wichita, KS 67213, USA*

[12]*Kyma Technologies Inc., Raleigh, NC 27617, USA*

[13]*Electronic Materials and Devices Department, Applied Research Laboratory, University Park, PA 16802, USA*

ABSTRACT: AlN thin films are enabling significant progress in modern optoelectronics, power electronics, and microelectromechanical systems. The various AlN growth methods and conditions lead to different film microstructures. In this report, phonon scattering mechanisms that impact the cross-plane (κ_z; along the c-axis) and in-plane (κ_r; parallel to the c-plane) thermal conductivities of AlN thin films prepared by various synthesis techniques are investigated. In contrast to bulk single crystal AlN with an isotropic thermal conductivity of ~330 W/mK, a strong anisotropy in the thermal conductivity is observed in the thin films. The κ_z shows a strong film thickness dependence due to phonon-boundary scattering. Electron microscopy reveals the presence of grain boundaries and dislocations that limit the κ_r. For instance, oriented films prepared by reactive sputtering possess lateral crystalline grain sizes ranging from 20 to 40 nm that significantly lower the κ_r to ~30 W/mK. Simulation results suggest that the self-heating in AlN film bulk acoustic resonators can significantly impact the power handling capability of RF filters. A device employing an oriented film as the active piezoelectric layer shows a ~2.5× higher device peak temperature as compared to a device based on an epitaxial film.

Keywords: Aluminum nitride, piezoelectric materials, thermal conductivity, MEMS resonators, thermal management

[a)] Author to whom correspondence should be addressed: sukwon.choi@psu.edu

1. INTRODUCTION

Aluminum nitride is an ultra-wide bandgap semiconductor that exhibits piezoelectricity and is utilized in optoelectronics, power electronics, and electro-acoustic applications.[1–4] For example, AlN-based deep ultraviolet (DUV) light-emitting diodes (LEDs) emitting at a wavelength of 210 nm have been demonstrated,[5] while alloying Ga (i.e., $Al_xGa_{1-x}N$) allows continuous spectral tuning to 400 nm. LED's operating in this UV-band support a wide range of applications such as water purification, UV sensors, and energy harvesting.[6] From a power electronics perspective, AlN's direct bandgap of ~6.2 eV and high breakdown field (>10 MV/cm) lead to a Baliga figure of merit (BFOM)[7] that is 34 times higher than that of GaN.[4] Electro-acoustically, AlN-based film bulk acoustic resonators (FBARs) have contributed to the performance enhancement and system size reduction of radio frequency (RF) signal processing applications[1] and telecommunication technologies[8]. A variety of AlN-based microelectromechanical systems (MEMS) such as surface acoustic wave (SAW) devices,[9] flexural plate wave (FPW) sensors,[10] micromachined ultrasonic transducers (pMUTs)[11], and contour mode resonators (CMRs)[12] have been commercialized.

To optimize the manufacturability and performance of AlN-based microsystems, several growth techniques have been employed. For DUV optoelectronic applications, large diameter high quality single crystal AlN wafers are desired. Physical vapor transport (PVT) is the most widely used approach for growing single crystal bulk AlN. Wafers with diameters up to 2-inches have been commercialized.[13,14] Several modified PVT methods have been developed to improve the crystal quality of bulk AlN.[15] For power electronic devices, including high-electron-mobility transistors (HEMTs), the growth of smooth and low defect density AlN films[16] is desired to form multilayered AlN/GaN/AlN[17] and AlN/AlGaN[18–20] heterostructures. Molecular beam epitaxy (MBE),[16,21] metalorganic chemical vapor deposition (MOCVD),[22] and hydride vapor phase epitaxy (HVPE)[23] have each been successfully used to grow high quality epitaxial AlN films on non-native substrates. AlN templates produced by these methods are also commonly used to produce epitaxial UV-C LEDs/detectors and high-power radio frequency (RF) electronic devices. These epitaxial growth methods require both high temperature growth conditions and single crystalline substrates to obtain epitaxial AlN films. For MEMS applications, growth of the piezoelectric thin film on metal electrodes is often needed and the growth temperature may be limited (<400 ˚C)[24] to be compatible with the complementary metal-oxide-semiconductor (CMOS) integrated circuit technology. Reactive sputtering is commonly used to synthesize oriented AlN thin films on a variety of growth templates at such moderate temperature ranges.[24] High quality, dense, c-axis textured AlN films have similar piezoelectric modulus (d_{33}) and elastic stiffness (C_{33}) as single crystal AlN and epitaxially grown films.[25–27] $Al_xGa_{1-x}N$-based DUV LEDs are often grown by MOCVD on high temperature-annealed sputter-deposited AlN/sapphire templates.[28]

High thermal conductivity is favored for engineering applications to mitigate device self-heating; however, the thermal conductivity of a thin film generally differs from its bulk counterpart. Bulk single crystal AlN exhibits a high thermal conductivity of ~320 W/mK at room temperature due to the strong interatomic bonding and the relatively light constituent elements.[29–31] The microstructure of a thin film is strongly affected by the substrate and the growth conditions, resulting in varying levels of crystallinity and point/extended defect densities.[24,32] For example, consider an AlN film prepared by sputter-annealing: AlN sputtered at modest temperatures typically exhibits a columnar structure with a small lateral grain size. These columnar grain domains combine and increase in size starting at 1300-1450°C. As the annealing temperature and/or time rises, the solid-state reaction continues to increase the grain size until around 1600-1750°C, where the previous columnar grain structure is transformed into a nearly grain boundary-free film. While the mechanism is not fully understood, oxygen is believed to have a significant role in the annealing process.[33] The film microstructure and finite thickness can limit heat conduction in the film due to increased levels of phonon scattering with point defects, dislocations, grain boundaries,

and film boundaries. For example, Xu *et al.*[34] reported a room temperature thermal conductivity of 237 ± 6 W/mK for bulk PVT-grown AlN with O, Si, C impurities with concentrations ranging from 0.4×10^{19} to 2×10^{19} cm^{-3}, and Al vacancies with concentrations of ~2×10^{19} cm^{-3}; this is significantly lower than the value calculated for pure AlN (~320 W/mK).[31] A detailed literature survey for thermal conductivity of bulk AlN with various defect and impurity concentrations has been reported by Inyushkin *et al*.[30] Xu *et al.*[34] also reported that 50% of the phonons of AlN (at room temperature) have mean free paths (MFPs) greater than ~0.3 μm and 10% of the phonons have long MFPs over ~7 μm. Taken in aggregate, the thermal conductivity of AlN will likely vary substantially when it is incorporated within a LED (e.g., bulk single crystal), a power switching transistor (i.e., epitaxial film), and a piezoelectric MEMS device (oriented film).

Owing to these expected differences, this work investigates the correlation between the microstructure and thermal conductivity of AlN thin films synthesized by different growth techniques. The implications on the thermal management and design of relevant device applications are assessed as well. Specifically, a commercial bulk AlN single crystal grown by PVT was prepared as a reference sample. The thermal properties of this single crystal reference were then compared to several industry-grade AlN thin films prepared by reactive sputter deposition, sputter-annealing, halide vapor epitaxy (HVPE), molecular beam epitaxy (MBE), and metal organic chemical vapor deposition (MOCVD). To understand the underlying causes for the variations in thermal properties observed, field emission scanning electron microscopy (FESEM), scanning transmission electron microscopy (STEM), energy dispersive x-ray spectroscopy (EDS), Raman spectroscopy, X-ray diffraction (XRD), and secondary ion mass spectrometry (SIMS) probed the crystallinity, defects, film stress, and microstructure. Finally, a device-level finite-element thermal model was used to demonstrate the significantly different level of self-heating in FBAR structures adopting oriented vs. epitaxial AlN thin films as the active piezoelectric layer.

2. RESULTS AND DISCUSSION

2.1. FILM CHARACTERIZATION

The cross-plane (κ_z) and in-plane (κ_r) thermal conductivities of the AlN films were measured by routine time-domain thermoreflectance (TDTR) and beam-offset TDTR, respectively.[35–37] Complementary techniques were used to validate results when applicable. For example, frequency-domain thermoreflectance (FDTR) measurements have been performed on pulse-DC reactive sputter-deposited samples and the results agreed with TDTR κ_z data within the error bar ranges (SP-157/Si: 18.3 ± 5.2 W/mK; SP-733/Si: 58.8 ± 6.1 W/mK). Steady-state thermoreflectance (SSTR), meanwhile, confirmed the thermal conductivity of the single crystal bulk sample producing a directionally averaged thermal conductivity of 292.4 ± 61.3 W/mK, which shows good agreement with the average of κ_z (330.1 ± 28.1 W/mK) and κ_r (326.5 ± 62.0 W/mK) acquired from TDTR measurements. SSTR was also used to extract the κ_r (230 ± 52.1 W/mK) of a HVPE-grown AlN film (HVPE-1083/Al_2O_3), based on the κ_z determined by TDTR measurements. The result agrees well with κ_r determined by beam-offset TDTR measurements. Together these results highlight the difference in thermal conductivities among the films are due to material variations and are not a measurement artifact.

TABLE 1 Summary of the characterization results. A positive residual stress means the film is under tensile stress.

	Growth Method	Substrate	Thickness (nm)	Grain Size (nm)	XRD FWHM (deg)	Raman FWHM (cm^{-1})	κ_z (W/mK)	κ_r (W/mK)	Stress (GPa)	Sample ID
Bulk single crystal	PVT	N/A	N/A	N/A		3.3 ± 0.02	330.1 ± 28.1	326.5 ± 62.0	0	PVT-Bulk
Epitaxial films	Sputter-annealing	(0001) Al_2O_3	394	N/A	0.016	3.90 ± 0.02	50.2 ± 16.6	115.5 ± 18.6	-1.24	SA-394/Al_2O_3

	Sputter-annealing	(0001) Al_2O_3	487	N/A	0.022	4.01 ± 0.05	89.2 ± 45.7	168.6 ± 17.0	-1.24	SA-487/Al_2O_3
	HVPE	(0001) Al_2O_3	1083	N/A	0.081	4.41 ± 0.02	96.2 ± 28.6	215 ± 34.0	-0.80	HVPE-1083/Al_2O_3
	MOCVD	(0001) 4H-SiC	967	N/A	0.062	3.90 ± 0.04	122.9 ± 16.1	286.4 ± 112.6	-0.84	MOCVD-967/SiC
	MBE	(111) Si	413	N/A	0.496	7.93 ± 0.57	104 ± 46	60.9 ± 23.0	0.37	MBE-413/Si
Oriented films	Sputtering	(001) Si	157	20.03	3.702	N/A	19.4 ± 4.8	N/A	N/A	SP-157/Si
	Sputtering	(001) Si	490	37.98	1.538	10.20 ± 0.22	42.8 ± 6.9	28.7 ± 15.2	0.43	SP-490/Si
	Sputtering	(001) Si	707	34.68	1.444	9.99 ± 0.14	79.6 ± 13.7	35 ± 9.9	0.30	SP-707/Si
	Sputtering	(001) Si	733	35.34	2.108	N/A	50.5 ± 6	39.3 ± 9.5	-0.16	SP-733/Si

Table 1 summarizes results of the thermal and structural characterizations performed on the AlN films. Each sample listed in **Table 1** is named based on the growth method, AlN film thickness, and substrate material. For example, SP-490/Si refers to a film deposited by reactive sputtering with a thickness of 490 nm, on a Si substrate. The thermal conductivity data presented in **Table 1** were measured by TDTR; the experimental details including the pump/probe spot sizes, sensitivity analysis, and error analysis are discussed in the EXPRIMENTAL SECTION/METHODS. The measured room temperature thermal conductivity of the bulk single crystal is nearly isotropic, with κ_r = 326.5 ± 62.0 W/mK and κ_z = 330.1 ± 28.1 W/mK; this agrees with the previously reported data for bulk AlN within the error bar ranges.[29,30,38] The cross-plane thermal conductivities of the AlN thin films show a strong correlation with the film thickness, as shown in **Figure 1 (a)**. The strong thickness dependence of κ_z is due to the relatively large population of long MFP phonons in AlN. Xu *et al.* calculated that 50% of the heat in pure, defect-free AlN is carried by phonons with MFPs greater than 0.3 μm and 10% is carried by phonons with MFPs longer than 7 μm at room temperature, as shown by the continuous line of **Figure 1 (a)**.[34] Freedman *et al.* measured the MFP spectra using broadband FDTR and reported that 50% of the thermal conductivity is contributed by phonons with MFPs greater than 2.5 μm at room temperature.[39] Overall, the measured κ_z values are lower than the theoretical predictions at the corresponding thicknesses due to additional phonon scattering mechanisms, which will be discussed in the following text. Nevertheless, the strong correlation between κ_z and thickness regardless of the film microstructure indicates the dominance of phonon-boundary scattering in sub-micrometer thick AlN films, as has been observed in GaN.[40]

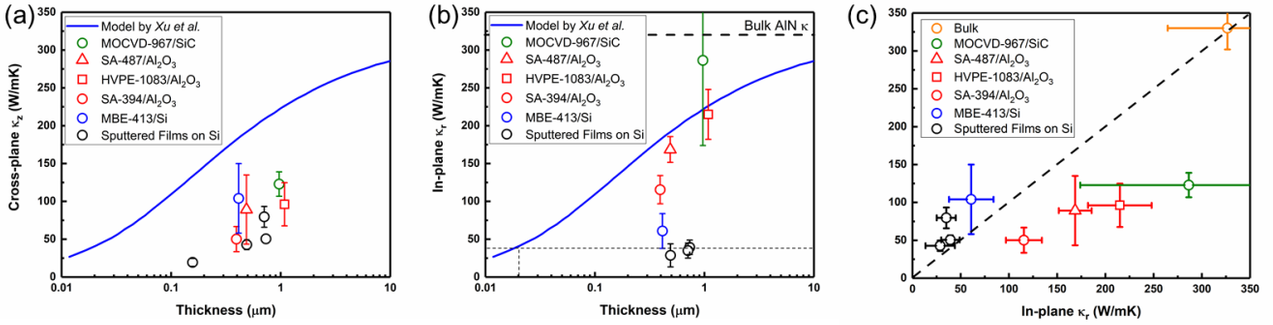

Figure 1. (a) The cross-plane thermal conductivity of the samples as a function of film thickness. The solid blue line plots the model predictions by Xu *et al.* for perfect single crystal AlN.[34] (b) The measured in-plane thermal conductivity of the AlN thin films. Also plotted is the bulk thermal conductivity of single crystal AlN[31] for comparison. The intersection of the blue line (cross-plane thermal conductivity calculations by Xu et al.[34]) and the gray dashed line corresponds to the thermal conductivity at a characteristic scattering length of 20 nm. (c) The cross-plane thermal conductivity versus the in-plane thermal conductivity of the AlN films and a bulk AlN substrate.

The in-plane thermal conductivities, however, do not show an apparent correlation with the film thickness; instead, they are dominated by the microstructures of the films. In other words, the anisotropy in the

thermal conductivities observed in the AlN thin films results from different scattering mechanisms that dominate phonon transport in the in-plane and cross-plane directions. **Figure 1 (c)** plots the κ_z values against the κ_r for the measured films. The dashed line is where κ_z equals to κ_r; therefore, the data points above the dashed line corresponds to films that possess a higher κ_z than κ_r, and the data below the dashed line are films with a κ_r larger than κ_z. While all the films show that κ_z is primarily limited by the finite film thickness (**Figure 1 (a)**), an interesting observation is that all the AlN films grown on Si have a higher κ_z than κ_r. As shown in **Figure 1 (b)**, the oriented films grown by pulsed-DC reactive sputtering possess a significantly lower κ_r than those for the epitaxial films. The reactive sputtering process produces c-axis textured polycrystalline films[24] that exhibit average lateral grain sizes ranging 20-40 nm as characterized by plan-view field emission scanning electron microscopy (FESEM) (**Figure 2 (a)**). When using the grain size (20 nm) as the characteristic scattering length, the measured κ_r agrees well with the model for a 20 nm thickness,[34] as shown by the vertical dashed line in **Figure 1 (b)**. Based on the observation that bulk single crystal AlN possesses an isotropic thermal conductivity, this indicates that the in-plane heat conduction in the oriented films is mainly limited by phonon-grain boundary scattering. Reactive sputtering of oriented AlN films is particularly important for fabricating CMOS compatible MEMS devices owing to the relatively low growth temperatures (<500 ˚C) and ability to grow on metal electrodes.[24] Industry-grade, dense c-axis textured AlN films possess a piezoelectric modulus (d_{33}) and elastic stiffness (C_{33}) comparable to those for epitaxial films and single crystal AlN.[25–27] Therefore, sputter-deposited films are favorable to be employed as the active piezoelectric layer of piezoelectric MEMS resonators. Recently, the electro-acoustic performance of FBAR band-pass RF filters based on physical vapor deposition (PVD)-sputtered c-axis oriented polycrystalline AlN films and MOCVD-grown epitaxial films was compared.[41] The devices based on MOCVD-grown epitaxial films were reported to have a 2.6 dB (or 18.1 W) higher power handling capability and a 0.2 dB lower insertion loss than those for RF filters based on sputter-deposited oriented films.[41] The results above suggest that the lateral heat spreading capability of the active AlN piezoelectric layer may significantly impact the power handling capability and energy loss of/within the MEMS resonators (to be discussed in sub-section 2.2).

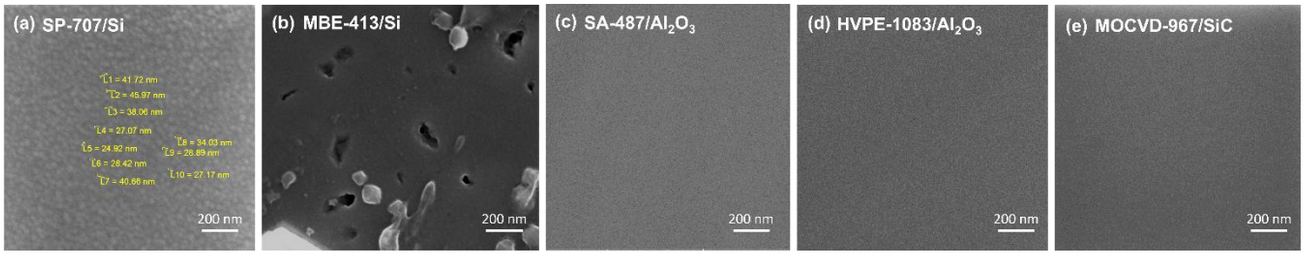

Figure 2. Representative plan-view FESEM images of the AlN samples. (a) Sputter-deposited oriented film on Si; *c*-axis textured grains are observed. (b) MBE-grown film on Si. (c) Sputter-annealed epitaxial film on a sapphire substrate. (d) HVPE-grown epitaxial film on sapphire. (e) Epitaxial film grown on a SiC substrate via MOCVD. The surface morphology of all epitaxial films grown on sapphire and SiC substrates (grown by sputter-annealing, HVPE, and MOCVD) were smooth and did not show the presence of pits, cracks, or large angle grain boundaries.

As discussed previously, the sputter-deposited oriented films on Si have *c*-axis oriented columnar grains with a small lateral grain size that limit the in-plane heat conduction due to phonon-grain boundary scattering. Interestingly, the MBE-grown film on Si also exhibits a relatively low κ_r, even though no lateral grain structure is observed in **Figure 2 (b)**. However, the scanning transmission electron microscopy (STEM) image of the MBE-grown AlN film suggests a significantly larger area density of dislocations (**Figure 3 (b)**, **(g)**) than that for epitaxial films grown on sapphire (HVPE and sputter-annealing) and SiC

substrates (MOCVD). This is likely due to the large lattice mismatch (19%) between the AlN (0001) and Si (111).[42,43] The strain formed by this lattice mismatch can be relieved by misfit dislocations as observed in the low-angle annular dark field (LAADF) STEM image shown in **Figure 3 (b)**. The MBE grown film is under a relatively low tensile stress (**Table 1**) due to this relaxation. The coefficient of thermal expansion (CTE) mismatch between (111) Si[44] ($2.6 \times 10^{-6} K^{-1}$ at room temperature) and AlN would also induce a tensile stress in the AlN film due to the high growth temperature of MBE (typically, ~1200 ˚C)[45]. Raghavan *et al.* calculated a 1000˚C drop from growth temperature would result in an AlN epitaxial film with a tensile stress of 0.9 GPa.[46] The high dislocation density observed in **Figure 3 (b), (g)** is thought to have further relaxed the strain and resulted in the relatively low tensile stress of ~0.4 GPa measured by Raman spectroscopy.

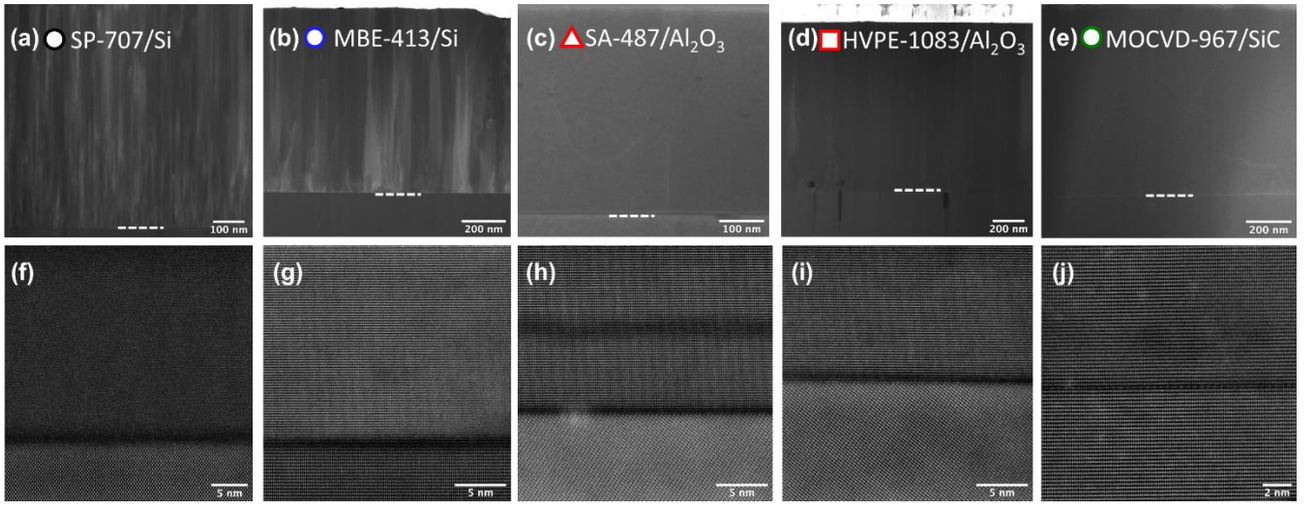

Figure 3. Representative LAADF-STEM images for a (a) sputter-deposited oriented film on Si, (b) MBE-grown film on Si, (c) a sputter-annealed epitaxial film on sapphire, (d) HVPE-grown epitaxial film on sapphire, and (e) the MOCVD-grown epitaxial film on SiC. Also shown are representative atomic resolution STEM images of the AlN/substrate interface for a (f) sputter-deposited oriented film on Si, (g) MBE-grown epitaxial film on Si, (h) sputter-annealed epitaxial film on sapphire, (i) HVPE-grown epitaxial film on sapphire, and (j) MOCVD-grown epitaxial film on SiC. All of the films show clear film/substrate interfaces. The color code for the sample IDs corresponds to the color code used in Figure 2.

According to **Figure 1 (b)**, the epitaxial films grown by sputter-annealing, HVPE, and MOCVD exhibit κ_r values that are far higher than those for the reactive sputtered and MBE-grown films. FESEM (**Figure 2 (c)** – **(e)**) and STEM images (**Figure 3 (c)** – **(e)**) show the absence of large angle grain boundaries or columnar grains in the epitaxial films. X-ray diffraction (XRD) and Raman spectroscopy were used to qualitatively compare the crystalline quality of all the samples. As shown in **Figure 4 (a)**, the epitaxial AlN films grown on sapphire and SiC substrates show narrower XRD full width at half maximum (FWHM) in the rocking curves than those for the films grown by reactive sputtering and MBE on Si, which indicates superior crystal quality. The MBE-grown film on a Si substrate shows a broader FWHM than the other epitaxial films, which supports the observation of a lower κ_r than those for SA-487/Al_2O_3 and SA-394/Al_2O_3 films of similar layer thicknesses (**Figure 1(b)**). This results in a different anisotropy in the thermal conductivity shown in **Figure 1 (c)** as compared to the other epitaxial AlN films. In contrast, the higher crystal quality for the epitaxial films on sapphire and SiC substrates supports the observation that κ_r is higher than κ_z of these films (**Figure 1 (c)**). The sputtered AlN films on Si substrates exhibit the

largest FWHM, consistent with a broader distribution of the crystallite orientations. Raman spectroscopy (**Figure 4 (b)**) confirms the findings from XRD measurements. For Raman measurements, the narrower FWHM of the E_2(high) peak indicates better crystalline quality.

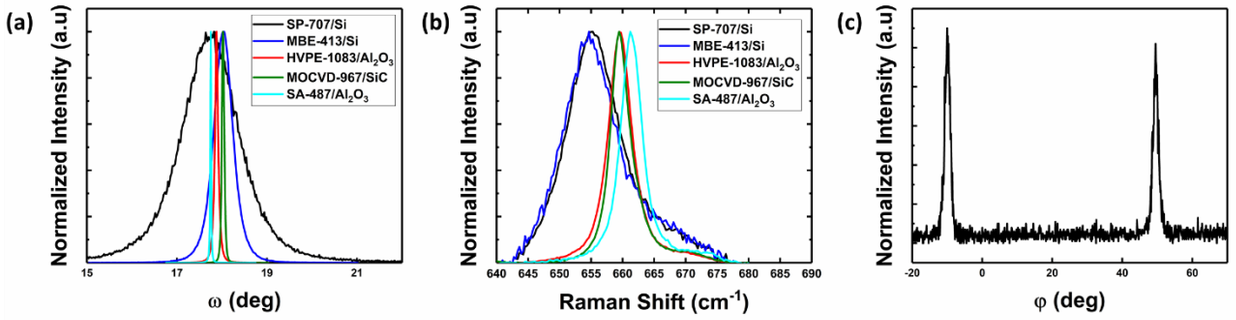

Figure 4. (a) XRD rocking curves showing the (002) AlN film peaks of the AlN films (b) Raman spectra of the AlN films showing the E_2(high) peak. All peaks are normalized with respect to the maximum intensity. The difference in Raman peak positions and linewidths between the two groups of the oriented films (sputtered, MBE) and epitaxial films (sputter-annealed, HVPE, MOCVD) show evidence supporting the difference in the crystalline quality and residual stress, respectively. (c) XRD φ scan for asymmetric planes of (102) of MBE-413/Si.

Among the epitaxial films, it should be noted that the MOCVD-grown film exhibits a κ_r that is comparable to a value predicted for single crystal bulk AlN (**Figure 1 (b)**); On the other hand, the films grown by MBE, sputter-annealing, and possess κ_r values that are considerably lower than the bulk thermal conductivity of single crystal AlN. To understand if the observed discrepancy is attributed to phonon-dislocation scattering, XRD measurements were performed on the epitaxial films to estimate their dislocation densities. The screw and edge dislocation densities of an AlN film were estimated from the full width at half maximum (FWHM) of the (002) and (102) XRD rocking curves, respectively, as shown below[47,48]:

$$\rho_e = \frac{\Delta\omega_{(102)}^2}{2\pi \ln(2)\, b_a^2} \tag{1}$$

$$\rho_s = \frac{\Delta\omega_{(002)}^2}{2\pi \ln(2)\, b_c^2} \tag{2}$$

The coefficients b_a and b_c are the magnitude of the corresponding Burger vector components; for the case of AlN they are the a and c lattice parameters, b_a = 0.3113 nm and b_c = 0.49814 nm.

The sputtered films only show the out of plane (002) peaks whereas no peak representing the (102) planes is observed in phi (φ) scans, indicating in-plane rotational disorder. Accordingly, the edge dislocation density could not be estimated. The XRD φ scan for (102) planes of the MBE-grown AlN film is shown in Figure 4 (c). The peaks separated by a 60° interval indicate the six-fold rotational symmetry of hexagonal AlN and confirm the in-plane (c-plane) periodicity, similar to what was observed in XRD φ scans for the epitaxial films grown by sputter-annealing, HVPE, and MOCVD.

Table 2 is a summary of the calculation results for the screw and edge dislocation densities of the epitaxial films. The MBE-grown AlN film exhibits the highest dislocation densities. These results confirm that the relatively low κ_r of MBE-413/Si among the epitaxial films is due to the high dislocation density. It should

be noted that the sputter-annealed AlN films (SA-394/Al_2O_3 and SA-487/Al_2O_3) exhibit the lowest dislocation densities among the epitaxial films. The improvement in the crystallinity of sputtered AlN films by high temperature annealing has been reported in literature.[33,49] However, their κ_r values are far lower than those for the HVPE- and MOCVD-grown films, which suggests that their in-plane heat conduction may be limited by other phonon scattering mechanisms such as phonon-point defect scattering.

Table 2 Dislocation densities calculated based on XRD rocking curve

	Edge Dislocation Density (cm^{-2})	Screw Dislocation Density (cm^{-2})
SA-394/Al_2O_3	3.36×10^8	6.19×10^6
SA-487/Al_2O_3	6.83×10^8	3.38×10^6
HVPE-1083/Al_2O_3	4.88×10^9	1.65×10^8
MOCVD-967/SiC	6.43×10^8	1.36×10^8
MBE-413/Si	1.06×10^{11}	7.54×10^9

An established scattering model (similar to the approach used in Beechem *et al.*[50]) was constructed to qualitatively study the effect of dislocation density on the AlN thermal conductivity. Results are shown in **Figure 5 (a)**. For simplicity, a combined effect of phonon scattering with screw and edge dislocations has been evaluated. Dislocations weakly affect the thermal conductivity up to a concentration level of ~10^8 cm^{-2}. MBE-413/Si exhibits significantly higher dislocation densities than the epitaxial films grown on SiC and Al_2O_3 due to the larger lattice mismatch between AlN and Si (19%); therefore, a lower κ_r was observed in this film as compared to other epitaxial films. SA-394/Al_2O_3 and SA-487/Al_2O_3 possess lower dislocation densities than HVPE-1083/Al_2O_3, due to the improved crystallinity from the high temperature annealing process.[51] However, it is worth noting that the κ_r of MOCVD-967/SiC is the highest among the AlN films tested even with higher dislocation densities as compared to these sputter-annealed samples; again, this is likely due to the additional phonon scattering mechanisms discussed in the following text. The dislocation density of the MOCVD-967/SiC is lower than the HVPE-grown film on Al_2O_3. This is attributed to the smaller lattice mismatch (~1%) between AlN and 4H-SiC.[52]

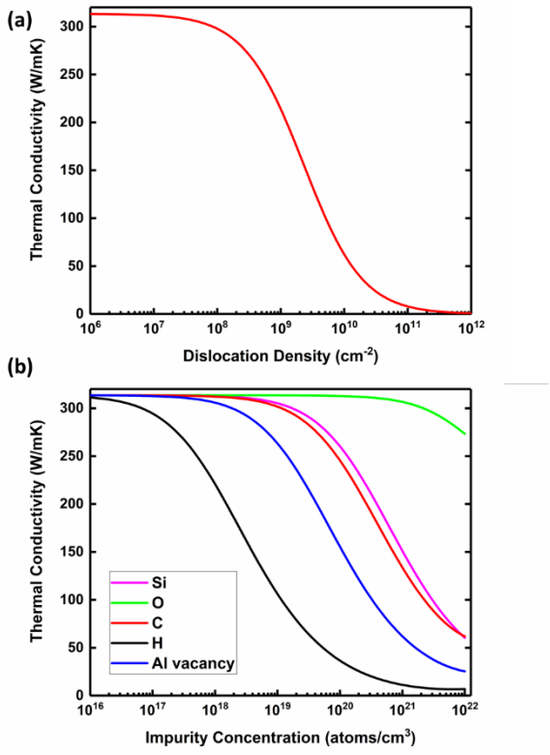

Figure 5. Thermal conductivity as a function of (a) the combined dislocation densities of the AlN film (b) the concentration of impurities and Al vacancies from simulation.

While the film thickness limits the cross-plane heat conduction and dislocations have a stronger effect on the in-plane thermal transport, point defects homogeneously scatter phonons traveling in all directions.[32,38,53,54] As seen in Figure 1 (a), the measured κ_z values for all of the AlN films are overall lower than the model prediction for a perfect AlN crystal with corresponding thicknesses. This suggests additional phonon-point defect scattering mechanisms may prevail. Such additional scattering events are also evidenced by the lower κ_r of all the epitaxial AlN films including MOCVD-967/SiC (286.4 ± 112.6 W/mK; with low dislocation density) as compared to that for bulk single crystal AlN (~319 W/mK)[31]. The κ_r of the sputter annealed samples are much lower than the bulk value even with the lowest estimated dislocation densities. The impurity concentrations of Si, O, C, H were characterized by secondary ion mass spectrometry (SIMS), and the thickness-averaged results are summarized in **Table 3**. The established scattering model[50] was further utilized to assess the impact of these impurities on phonon scattering, and hence on the AlN thermal conductivity. Results are summarized in **Figure 5 (b)**. It should be noted that H concentrations are higher in the oriented films; modeling results show H interstitial impurities with a concentration above ~10^{18} atoms/cm^3 can significantly reduce the thermal conductivity. However, the thermal conductivities of the epitaxial films are expected to be less impacted by H impurities due to their overall lower concentrations. C and Si impurities are predicted to weakly impact the thermal conductivity below concentration levels of 10^{20} atoms/cm^3. This is because Si has a similar atomic mass and ionic radius as Al.[55,56] Also, the difference between the atomic mass and ionic radius of C and Al is much smaller than the case of H and Al. The overall low levels of C and Si impurity concentrations of the tested samples rule out the possibility for these impurities to significantly reduce the thermal conductivities. For a similar reason, the O substitutional impurities on the N site are predicted to have a relatively weak effect on the thermal conductivity due to the similar atomic masses and ionic radii.

This is not to say that O does not affect the thermal conductivity. Rather, previous studies have suggested that Al vacancies forming in response to this O substitutional process can have a strong effect on the thermal conductivity (and the piezoelectric response[57]) of AlN.[31,58] When O atoms enter the AlN lattice, it is energetically favorable for them to replace the N sites; this process leaves one Al vacancy (V_{Al}) for every three O atoms incorporated into the lattice.[54,58] The Al vacancies, in turn, create large mass and size differences with respect to the original lattice and therefore significantly reduce the thermal conductivity. Notably, the MOCVD-967/SiC and MBE-413/Si samples, which have the lowest O concentrations, also exhibit the highest cross-plane thermal conductivity for the films at comparable thickness, as shown in Figure 1 (a). O contamination is commonly found in AlN thin films grown by various techniques because O atoms exhibit a higher affinity than N towards Al atoms.[59,60] The O impurity concentrations in the HVPE-grown sample and the sputter annealed films are observed to be four orders of magnitude higher than that for the MOCVD-grown film. This explains why these epitaxial films with comparable or even lower dislocation densities exhibit lower κ_r values than the MOCVD-grown sample. In fact, the incorporation of O is common for all the growth techniques discussed. For example, multiple sources of O contamination have been reported for the HVPE growth process. These include the quartz-made aluminum boat reacting with the AlCl precursor, the aluminum oxide that remains in the source boat after HCl activation, and the residual contamination of the source gases.[61] O impurities in PVT-grown AlN mainly come from the Al_2O which is a major gas-phase species in the growth chamber.[62] For sputter deposition, the O contamination can be caused by residual gas molecules remaining that are not completely removed from the vacuum chamber.[59,63] For this reason, Al vacancies are thought to be responsible for both the κ_r and κ_z of all samples to be lower than the calculated values for a perfect crystal (**Figure 1 (a)**, **(b)**).

TABLE 3 Impurity concentrations (atoms/cm^3) of O, H, C, and Si

	Sample ID	Substrate	O	H	C	Si
Single crystal bulk	PVT-Bulk	N/A	1.0×10^{18}	1.3×10^{17}	9.1×10^{18}	9.8×10^{19}
Epitaxial films	SA-394/Al_2O_3	(0001) Al_2O_3	2.6×10^{20}	9.6×10^{18}	1.1×10^{18}	8.5×10^{18}
	SA-487/Al_2O_3	(0001) Al_2O_3	1.3×10^{20}	2.0×10^{17}	7.8×10^{17}	7.5×10^{18}
	HVPE-1083/Al_2O_3	(0001) Al_2O_3	1.4×10^{20}	2.5×10^{17}	2.3×10^{16}	1.7×10^{18}
	MOCVD-967/SiC	SiC	5.1×10^{16}	3.4×10^{17}	2.8×10^{16}	3.0×10^{17}
	MBE-413/Si	(111) Si	2.3×10^{17}	2.9×10^{17}	1.0×10^{16}	4.2×10^{19}
Oriented films	SP-490/Si	(001) Si	3.9×10^{18}	4.0×10^{19}	3.8×10^{17}	5.6×10^{17}
	SP-707/Si	(001) Si	6.1×10^{18}	7.7×10^{18}	9.1×10^{17}	4.7×10^{17}

It should be noted that oxygen can be intentionally incorporated into AlN films for ultraviolet (UV) optoelectronic applications. As shown in **Figure 6 (b)**, energy dispersive x-ray spectroscopy (EDS) mapping shows an oxygen concentrated layer near the AlN/substrate interface of a sputter-annealed AlN sample (SA-394). This oxygen rich layer is also shown in the elemental maps in **Figure 6 (a)**. Sapphire is often used as a UV-transparent substrate for optoelectronic applications based on AlN and $Al_xGa_{1-x}N$. The aluminum oxynitride (AlON) layer near the interface improves index matching for better optical extraction from UV LEDs.[64] However, from a thermal management perspective, this AlON layer potentially hinders heat extraction through chip packaging and may result in additional device self-heating that can compromise the maximum achievable power, efficiency, and lifetime of the LEDs.[6] Therefore, it may be important to consider phonon scattering caused by the low thermal conductivity AlON layer (~10 W/mK)[65,66] when designing thermal management solutions for optoelectronic devices.

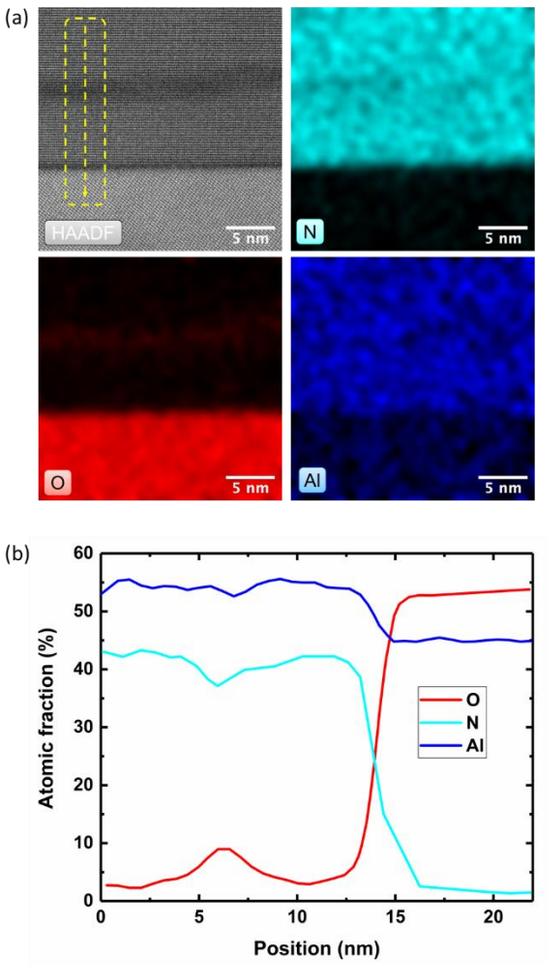

Figure 6. (a) STEM-EDS elemental map of the SA-394 sample from the cross-section. An oxygen rich layer was observed ~10 nm above the interface. (b) Line scan of the EDS data along the yellow dashed line shown in (a), from the AlN film towards the Al_2O_3 substrate.

2.2. DEVICE SELF-HEATING

It is clear from the preceding data that that thermal conductivity is closely linked to the growth technique used to synthesize the AlN films. Here, it is shown that these changes in thermal conductivity have a practical impact on device applications. A 3-dimensional (3D) finite-element thermal model of a film bulk acoustic resonator (FBAR) was created using COMSOL Multiphysics.[67] AlN was used as the active piezoelectric layer of two FBAR devices with identical geometry but with different thermal conductivities, corresponding to the measured values for sputter-deposited and MOCVD-grown AlN films. The film thicknesses were both assumed to be 800 nm, yielding a fundamental thickness-mode resonance frequency of ~4 GHz.[68] The active area is 85 μm × 85 μm to give a 50 Ω capacitive impedance at the resonant frequency. A square device shape was assumed to simplify calculations for the thermal performance. A mapped mesh was used with maximum element size of 5 μm for the active area. For the bulk geometry, the mesh was built by using a user-defined fixed number of elements to properly simulate the domain while managing the computational cost. A stationary, direct solver was used to calculate the device temperature rise. A power vs. device temperature study was performed for three existing and

potential applications. Assuming 1 / 20 / 50 W of transmit power (for mobile, base station, and military radar applications, respectively), a filter insertion loss of 2 dB per resonator, and 8 resonators in the ladder filter, 0.046 / 0.92 / 2.3 W is dissipated per resonator. Uniform volumetric heat generation corresponding to these values was applied to the active region of the FBAR models. All the dissipated energy was assumed to convert to heat within this volume, and therefore the simulated temperatures represent the upper bound of self-heating. A schematic of the simulated FBAR cross section is shown in **Figure 7 (a)**. The bottom of the Si substrate was assumed to be at room temperature. Natural convection, represented by a heat transfer coefficient of 10 W/m^{2}K, was used as a thermal boundary condition for all other surfaces. Two case studies were performed using measured anisotropic thermal conductivity values for oriented and epitaxial AlN films with thicknesses close to 800 nm (i.e., the sputter-deposited oriented film shown in **Figure 7 (b)** and the MOCVD-grown epitaxial film illustrated in **Figure 7 (c)**). The lower thermal conductivity of the sputtered film resulted in a 50 K higher peak temperature rise (85 K) as compared to the device based on a MOCVD film (35 K) for mobile applications. The electro-acoustic performance of FBAR band-pass RF filters based on c-axis oriented polycrystalline AlN films and epitaxial MOCVD grown-films has been reported elsewhere.[41] Filters based on MOCVD-grown epitaxial AlN films exhibited the highest reported power handling capability (46.1 dBm or 40.6 W) for bulk acoustic wave (BAW) RF filters at the mid-3 GHz frequency range. A device based on MOCVD-grown AlN exhibited a 2.6 dB or 18.1 W higher power handling capability and a 0.2 dB lower insertion loss compared to RF filters based on oriented sputtered films. Therefore, the modeling data in **Figure 7** suggest that the thermal conductivity of the active piezoelectric layer may significantly impact the energy loss (e.g., via Akhiezer damping[69]) and power handling capability of piezoelectric MEMS resonators.

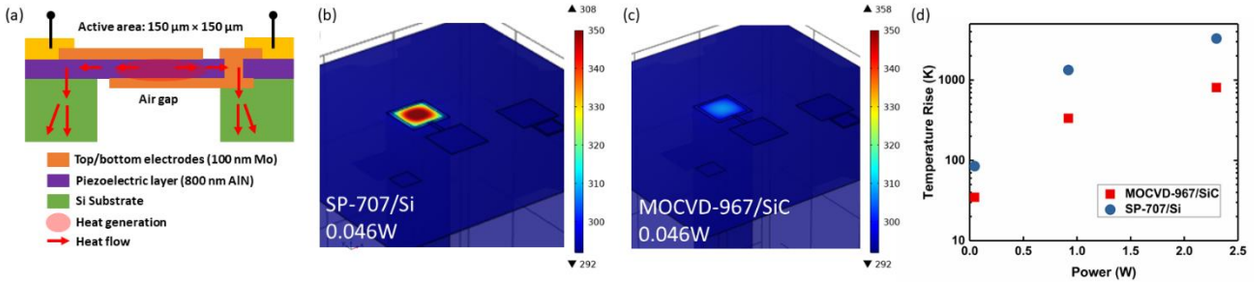

Figure 7. (a) Cross-sectional schematic of the simulated AlN FBARs. Device modeling results for AlN FBARs based on (b) a sputter-deposited oriented film and (c) a MOCVD-grown epitaxial film. (d) The peak temperature rises of simulated FBARs as a function of dissipated power for mobile, base station, and military radar applications.

3. CONCLUSIONS

In this study, thermal/structural characterizations on AlN thin films synthesized by different growth techniques was performed. The cross-plane heat conduction in the AlN thin films is limited by the phonon-boundary scattering due to the relatively large population of acoustic phonons with long MFP present in AlN. The lowest in-plane thermal conductivity was observed in the *c*-axis oriented sputtered AlN films. This may impose drive level limitations on the AlN piezoelectric layer in piezoelectric MEMS resonators prepared via reactive sputtering, that may limit the power handling capability. Epitaxial films grown by sputter-annealing, HVPE, and MOCVD exhibit higher in-plane thermal conductivities. The in-plane thermal conductivity of an epitaxial film is strongly affected by the dislocation density, as observed in a film grown on a Si substrate. Impurity concentrations in the films were characterized by SIMS and a

thermal conductivity model suggests that Al vacancies decreases the thermal conductivity of a AlN thin film substantially. Finally, a 3D finite-element thermal model was constructed to study the self-heating behavior of FBARs based on a sputter-deposited textured AlN film and an epitaxial film. Simulation results indicate that overheating in devices based on sputter-deposited films can limit their use in high power applications. The outcomes of this work provide insight into the importance of using appropriate thermal properties for the modeling and design of AlN-based microsystems; for example, using the bulk thermal conductivity of AlN will significantly underestimate the temperature rise in relevant AlN thin film-based technologies.

EXPERIMENTAL METHODS

AlN film synthesis

SP-157/Si, SP-707/Si, SP-733/Si: This series of AlN films were reactively sputtered using a SPTS Sigma 200 deposition system with an Al target. Deposition conditions are like those found in reference[70]. Sample SP-707 differs from others since it used 100% N_2 gas during deposition (others were made with an Ar/N_2 mixture) and had a pre-sputter etch before AlN deposition, which allowed the film to achieve a higher crystallographic texture.

SP-490/Si: The 490 nm of sputtered AlN was deposited directly onto Si <100> wafers using an Al target and a N_2/Ar gas mixture at a chuck temperature of 300°C.

SA-487/Al_2O_3: The sputter-annealing process has been well-described by Uesugi *et al.*[71] Aluminum was reactively sputtered in a nitrogen plasma onto the sapphire substrate at temperatures higher than 1000°C. The sputtering process forms AlN columns with relatively high levels of threading dislocations. Initial rocking curves for the (102) plane in the as-sputtered films have FWHM that generally exceed 2000 arcsec. The sputtered templates are then annealed at temperatures above 1500°C for several hours, resulting in healing of dislocations and a large reduction in the FWHM value to less than 300 arcsec.

SA-394//Al_2O_3: This sputter-annealed sample with a thickness of 394 nm was prepared using DC reactive magnetron sputtering of AlN onto a sapphire substrate using a pure Al target and sputtering in argon and nitrogen. After growth, the films were annealed for 2 hours under a nitrogen overpressure at a nominal temperature of 1650°C in order to improve its structural quality as reported in reference[71].

HVPE-1083/Al_2O_3: Aluminum nitride (AlN) was grown on a c-plane sapphire substrate by HVPE. The deposition utilized a two zone inductively heated hot-wall reactor capable of temperatures exceeding 1500°C. During the process, $AlCl_3$ gas was formed in the first zone by flowing HCL in a nitrogen carrier gas over high-purity aluminum pellets, and then the $AlCl_3$ gas mixture was introduced into a high temperature zone where it impinged on the sapphire substrate in the presence of anhydrous NH_4, forming the final AlN film. This film has a low level of dislocations, with typical FWHM values less than 400 arcsec for the (102) plane, and less than 300 arcsec for the (002) plane.

MBE-413/Si: Plasma- MBE was used for growth of AlN. Aluminum was evaporated from an effusion cell and activated nitrogen was introduced from a plasma source. A high purity 100 mm <111> orientation float-zone (FZ) Si wafer (resistance 3000 Ω·cm) was used as the substrate. More details on the epitaxial growth process are available elsewhere[72].

MOCVD-967/SiC: The MOCVD-grown AlN was deposited onto a semi-insulating 4H-SiC substrate in a single deposition step at 1250°C using trimethylaluminum (TMAl) and NH_3 precursors. The properties of this material is discussed in[41].

Scanning electron microscopy (SEM) imaging

Scanning electron microscopy (SEM) was used to characterize the film microstructure.[73] Topside imaging was performed under high vacuum in a Tescan MIRA3 SEM with an Everhart-Thornley secondary electron (SE) detector.

Scanning transmission electron microscopy (STEM)

STEM samples were prepared using FIB (Thermofisher Helios Dual-beam FIB). To retain a clean and thin specimen, the surface of the STEM foils was cleaned using low-energy ion milling (Fischione Nanomill) operated at 500 eV. Both high-angle and low-angle annular dark-field (HAADF and LAADF, respectively) STEM imaging were performed using a Thermofisher aberration-corrected Titan scanning transmission electron microscope with a probe convergence half angle of 10.03 mrad at an accelerating voltage of 300 kV. The microscope is also equipped with a ChemiSTEM EDX system, which allows for the characterization of the composition of the cross-sectional STEM sample. Three chemical species (O, Al, and N) at the interface were analyzed by the EDX elemental mapping.

X-ray diffraction (XRD)

X-ray diffraction (XRD) was used to confirm the phase and orientation as well as assess the crystalline quality of the AlN films. High-resolution scans were collected using a Malvern Panalytical Materials Research Diffractometer (MRD) system in line focus mode with Cu $K_{\alpha 1}$ radiation. 2-Theta (2Θ) scans were obtained over a wide range (10-70° 2Θ) to verify the phase and identify the film and substrate peaks. The detector (PIXcel 3D; beam mask = 10 mm; divergence slit = ¼ degree) was aligned to the (002) AlN film peak at approximately 35.796° 2Θ by collecting successive omega (ω) and chi (χ) scans over progressively narrow ranges to optimize the sample tilt by maximizing intensity. A rocking curve or ω scan was collected over a range of 2.000° with a 0.005° step size and dwell time of 0.100 s. The φ-scan for (102) planes was collected over a range of 100.00° with a 0.1° step size and a dwell time of 0.100 s. Note that the range and step size were increased for the samples with a Si substrate. The full-width-at-half-maximum (FWHM) was calculated for each rocking curve, where a lower value generally implies superior crystalline quality.

Raman Spectroscopy:

To assess the crystalline quality of the AlN epitaxial films, room temperature Raman spectra were collected using a Horiba LabRAM HR Evolution spectrometer equipped with an excitation laser of 532 nm and an 1800 grooves/mm grating. A long working distance 50× objective (NA = 0.45) was used to probe the samples. According to the energy-time uncertainty principle, as the crystalline quality decreases, the linewidth of the E_2(high) phonon mode will increase because of decreased phonon lifetime. Therefore, the E_2(high) linewidth was used to qualitatively compare the crystalline quality of the AlN samples. In addition, the film residual stress was quantitatively measured with Raman spectroscopy with recently published work.[74] The peak shift in the E_2(high) mode with respect to a stress-free phonon frequency of 656.68 cm^{-1} (measured from the bulk single crystal AlN sample in **Table 1**) is monitored and the difference is converted to biaxial stress using a stress coefficient of -3.8 cm^{-1}/GPa.[74] The system is initially calibrated to single crystal Si peak at 520.7 cm^{-1}. A mercury emission line at ~480 cm^{-1} was used as a reference to monitor and compensate the instrument drift from error sources such as room temperature fluctuations. A low laser power ~1 mW was used to measure films on Si substrate to avoid heating in the Si due to the lower bandgap energy as compared to the laser energy (~2.33 eV).[74] The Raman peak intensity for SP-157/Si was too low to obtain meaningful results due to the low thickness of this sample.

Time Domain Thermoreflectance (TDTR):

The sample thermal conductivities were measured with TDTR.[36] Prior to TDTR thermal measurements, an ~80 nm thick transducer layer (Au / Al) was deposited onto the sample to serve as the transducer. In

TDTR, a Ti:sapphire ultrafast laser produces a train of pulses at a repetition rate of 80 MHz, which is separated into a pump beam and a probe beam by a polarizing beam splitter. A double-modulation scheme is adopted to improve the measurement reliability, where the pump beam is modulated by an electro-optical modulator and the probe beam is modulated by a mechanical chopper. A delay stage varies the optical path of the pump beam, producing a time delay of up to 4 ns between pump heating and probe sensing, as a typical pump-probe configuration. The reflectivity of the probe beam from the sample surface is collected by a photodiode, which is used for data reduction to extract the sample thermal conductivity and interfacial thermal conductance between the Al transducer and the sample beneath (provided sufficient measurement sensitivity to the thermal interface). For the cross-plane thermal conductivities of AlN films, routine TDTR measurements were taken at a modulation frequency of 9 MHz and with a larger beam spot (a 5× objective lens for sputtered films which produces a $1/e^2$ radius of 12 μm, and a 10× objective lens for epitaxial films which yields a radius of 6 μm). A smaller beam spot size was used for the epitaxial films with Au transducers because Au has a lower thermoreflectance coefficient than Al at the 780 nm[75] wavelength and thus necessitates a smaller beam spot size and higher laser powers to improve the signal amplitudes. The powers of the pump and probe beams were carefully tuned to ensure a good signal-to-noise ratio with moderate steady-state heating for all sample stacks at room temperature. The cross-plane thermal conductivities of the samples are extracted by fitting the TDTR ratio signals ($-V_{in}/V_{out}$) to a heat diffusion model. For in-plane thermal conductivities, beam-offset measurements were conducted at 1.51 MHz with a 20× objective lens ($1/e^2$ radius of 3 μm) to maximize the measurement sensitivity to in-plane thermal transport.[76–78] The FWHM of the out-of-phase signal (V_{out}) at -50 ps from beam-offset measurements was compared with that predicted from the heat diffusion model to determine the in-plane thermal conductivities of AlN thin films. The values of κ_z obtained from routine TDTR served as input parameters in the data reduction of in-plane beam-offset measurements.

The error bars of the in-plane thermal conductivities (κ_r) of the AlN samples were calculated based on the sensitivity analysis of the beam-offset measurements as follows:[37,77,78]

$$S_\alpha = \frac{\partial \ln(\mathrm{FWHM})}{\partial \ln(\alpha)}$$

$$\frac{\delta \kappa_r}{\kappa_r} = \sqrt{\sum_\alpha \left(\frac{S_\alpha}{S_{\kappa_r}} \frac{\delta \alpha}{\alpha}\right)^2}$$

where FWHM is the full width at half maximum of the out-of-phase signal from the beam-offset measurements. α stands for certain parameters in the thermal model that also act as individual error sources, including the beam spot size (w_0), thicknesses (h_{tran}, h_{AlN}), heat capacities (C_{tran}, C_{AlN}, C_{sub}), interfacial thermal conductance (G_1 at the transducer/AlN interface and G_2 at the AlN/substrate interface), and thermal conductivities (κ_{tran}, through-plane κ_z of AlN, in-plane κ_r of AlN, κ_{sub}). Errors from parameters other than κ_r will propagate into the total uncertainty of κ_r. Representative examples for modeling parameters and their percent errors are summarized in **Table 4**; it should be noted that the transducers used for MOCVD-967/SiC (Al) and HVEP-1083/Al_2O_3 (Au) are different and therefore the corresponding errors in the properties vary. The sensitivity of each modeling parameter is plotted in **Figure 8**. The uncertainties of each modeling parameter can propagate into the fitting results for the thermal conductivity based on their corresponding sensitivity. For example, the larger in-plane thermal conductivity uncertainty of the MOCVD-967/SiC can be attributed to the larger sensitivities of the other parameters that propagates error into the fitting.

The pump laser spot sizes were large enough to capture the impacts of different scattering mechanisms for each film. For instance, the heating area is similar to the pump size (3-12 μm for TDTR), which is orders of magnitude larger than the averaged grain size (20-40 nm). At this pump radius, the impacts of dislocations are also sufficiently captured as their densities are on the order of 10^8 – 10^{11}/cm^2.

Table 4: Summary of individual parameters with error sources (%) for MOCVD-967/SiC and HVPE-1083/Al_2O_3.

Sample ID	h_{tran} (nm)	h_{AlN}	C_{tran} (MJ/m^{3}K)	C_{AlN}	C_{sub}	G_1 (MW/m^{2}K)	G_2	κ_{tran} (W/mK)	κ_z of AlN	κ_{sub} (W/mK)	w_0 (μm)
MOCVD-967/SiC	71 (3%)	967.2 (3%)	2.42 (3%)	2.38 (3%)	2.21 (3%)	38 (5.6%)	200 (20%)	89.5 (3%)	122.9 (13%)	324.8 (10%)	≈3 (2%)
HVPE-1083/Al_2O_3	81.3 (1.2%)	1083 (3%)	2.46 (1.2%)	2.38 (3%)	3.03 (3%)	22 (5.4%)	400 (20%)	200 (1.2%)	96.2 (29.7%)	32.1 (12%)	≈3 (2%)

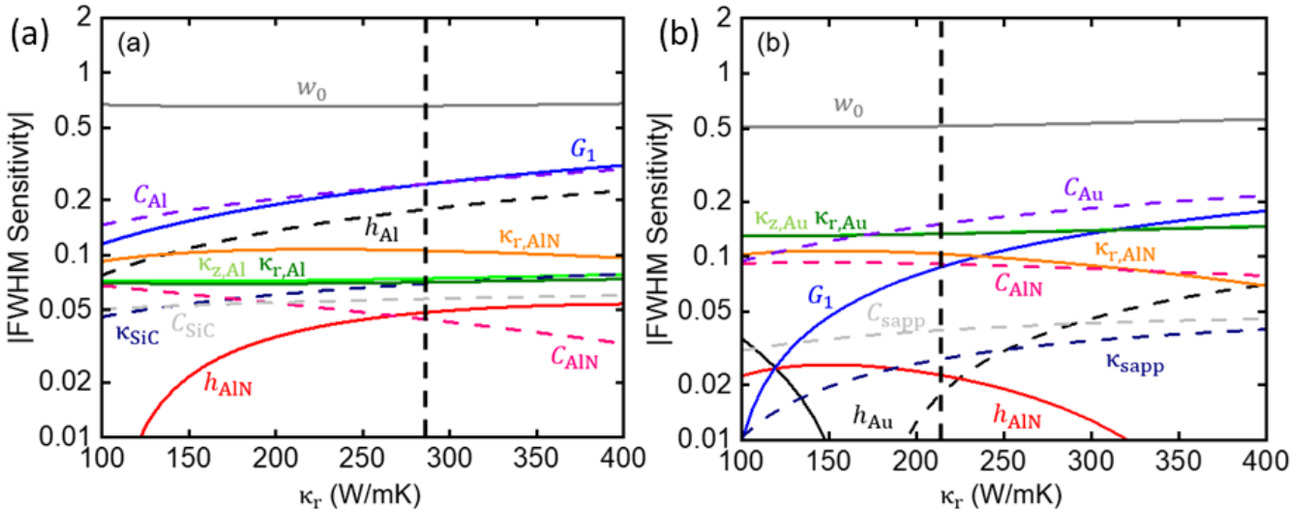

Figure 8. Sensitivity analyses of the beam-offset measurements to individual parameters for (a) MOCVD-967/SiC and (b) HVPE-1083/Al_2O_3.

Thermal Conductivity Measurements (FDTR):
FDTR is an optical pump-probe technique that extracts material thermal properties from the phase response of the thermal wave over a range of modulation frequencies[79]. The detailed setup of the FDTR used in this study has been described in the previous work[70]. The radius of the focused pump and probe beams were 13.4 μm and 13.1 μm, respectively. Material properties used in the FDTR fitting model were identical to those used in the TDTR model.

Thermal Conductivity Measurements (SSTR):
SSTR is a laser-based pump-probe technique that extracts the material thermal conductivity based on Fourier's law of heat transfer.[80] The detailed setup of the SSTR used in this study has been described in previous work.[81] The radius of the focused pump and probe beams were 19.9 μm and 12.4 μm, respectively. SSTR does not require heat capacity information for the materials since to the pump laser heating occurs under steady state. Single crystal Si (135 W/mK) and sapphire (31 W/mK) were used as calibration samples with known thermal conductivities. SSTR is well suited for measuring the directionally averaged thermal conductivity of bulk materials and was used to characterize a single crystal bulk AlN substrate in this work. It is also possible to extract the in-plane thermal conductivity of a thin-film when the film has a much higher thermal conductivity than the substrate material, as recently demonstrated by Hoque et al.[38] A similar approach was used to extract the in-plane thermal conductivity of HVPE-1083/Al_2O_3, where the cross-plane thermal conductivity measured by TDTR was used as a

known fitting parameter in the model used to extract the in-plane thermal conductivity. Measurements were performed on 3 random spots on the sample and were averaged over 30 data points at each power level.

Secondary Ion Mass Spectrometry (SIMS):
Secondary ion mass spectrometry measurements were performed using a commercial vendor (Evans Analytical Group).

THEORETICAL CALCULATIONS

The thermal conductivity is calculated via the approach described by Beechem et al.[50] The thermal conductivity is calculated with[50]:

$$\kappa = \frac{1}{6\pi^2}\sum_s \int_0^{q_{m,s}} \frac{\hbar^2\omega^2(q)}{\kappa_B T^2} \frac{\exp\left(\frac{\hbar\omega(q)}{\kappa_B T}\right)}{\left[\exp\left(\frac{\hbar\omega(q)}{\kappa_B T}\right)-1\right]^2} \nu^2(q)\tau_s(q)q^2 dq$$

where q is the wavevector, ħ is the modified Planck's constant, ω is the phonon frequency, κ_B is the Boltzmann constant, ν is the group velocity, and τ is the scattering time. All phonon branches were summed over for the Γ-A direction, representing the cross-plane thermal conductivity. The scattering term τ includes Umklapp scattering τ_U, boundary scattering, τ_B, and impurity scattering, τ_I. The impurity scattering τ_I discussed in this study is calculated based on the mass and size difference of the impurity atoms as compared to the original lattice. The mass difference for the vacancies are accounted for by assuming the mass to be double that of the missing atom.[82] Pauling ionic radius of the individual defects was used for calculating the strain induced by impurities due to size difference. The method is adopted from reference.[56]

ACKNOWLEDEGMENTS

This material is based upon work supported by the National Science Foundation, as part of the Center for Dielectrics and Piezoelectrics under Grant Nos. IIP-1361571, IIP-1361503, IIP-1841453, and IIP-1841466. C.Z., Y.Z., and X.W. greatly appreciate the support from the MN Futures Award and NSF (under Award No. 1804840). H. H., C. C., and J. H. were supported by the Department of Defense, Air Force Office of Scientific Research GAME MURI Program (Grant No. FA9550-18-1-0479). Electron microscopy was performed at the Center for Electron Microscopy and Analysis at The Ohio State University. T.M. and J.M.R. were supported by AFOSR under Award FA9550-19-1-0349. This work was performed, in part, at the Center for Integrated Nanotechnologies, an Office of Science User Facility operated for the U.S. Department of Energy (DOE) Office of Science. Sandia National Laboratories is a multimission laboratory managed and operated by National Technology & Engineering Solutions of Sandia, LLC, a wholly owned subsidiary of Honeywell International, Inc., for the U.S. DOE's National Nuclear Security Administration under contract DE-NA-0003525. The views expressed in the article do not necessarily represent the views of the U.S. DOE or the United States Government.

DATA AVAILABILITY

The data that support the findings of this study are available from the corresponding author upon reasonable request.

REFERENCES

[1] G. Piazza, V. Felmetsger, P. Muralt, R.H. Olsson III, and R. Ruby, MRS Bull. **37**, 1051 (2012).
[2] E. Iborra, J. Olivares, M. Clement, L. Vergara, A. Sanz-Hervás, and J. Sangrador, Sensors Actuators, A Phys. **115**, 501 (2004).
[3] P. Nicolay, O. Elmazria, B. Assouar, F. Sarry, and L. Lebrizoual, Proc. - IEEE Ultrason. Symp. 272 (2007).
[4] J.Y. Tsao, S. Chowdhury, M.A. Hollis, D. Jena, N.M. Johnson, K.A. Jones, R.J. Kaplar, S. Rajan, C.G. Van de Walle, E. Bellotti, C.L. Chua, R. Collazo, M.E. Coltrin, J.A. Cooper, K.R. Evans, S. Graham, T.A. Grotjohn, E.R. Heller, M. Higashiwaki, M.S. Islam, P.W. Juodawlkis, M.A. Khan, A.D. Koehler, J.H. Leach, U.K. Mishra, R.J. Nemanich, R.C.N. Pilawa-Podgurski, J.B. Shealy, Z. Sitar, M.J. Tadjer, A.F. Witulski, M. Wraback, and J.A. Simmons, Adv. Electron. Mater. **4**, 1600501 (2018).
[5] Y. Taniyasu, M. Kasu, and T. Makimoto, Nature **441**, 325 (2006).
[6] M. Kneissl, T.-Y. Seong, J. Han, and H. Amano, Nat. Photonics **13**, 233 (2019).
[7] B.J. Baliga, J. Appl. Phys. **53**, 1759 (1982).
[8] G. Piazza, V. Felmetsger, P. Muralt, R.H. Olsson, and R. Ruby, MRS Bull. **37**, 1051 (2012).
[9] C. Li, X. Liu, L. Shu, and Y. Li, Mater. Express **5**, 367 (2015).
[10] M. Reusch, K. Holc, L. Kirste, P. Katus, L. Reindl, O. Ambacher, and V. Lebedev, Procedia Eng. **168**, 1040 (2016).
[11] J. Jung, W. Lee, W. Kang, E. Shin, J. Ryu, and H. Choi, J. Micromechanics Microengineering **27**, (2017).
[12] G. Piazza, P.J. Stephanou, and A.P. Pisano, J. Microelectromechanical Syst. **15**, 1406 (2006).
[13] T.Y. Chemekova, O. V Avdeev, I.S. Barash, E.N. Mokhov, S.S. Nagalyuk, A.D. Roenkov, A.S. Segal, Y.N. Makarov, M.G. Ramm, S. Davis, G. Huminic, and H. Helava, Phys. Status Solidi C **5**, 1612 (2008).
[14] S.B. Schujman, L.J. Schowalter, R.T. Bondokov, K.E. Morgan, W. Liu, J.A. Smart, and T. Bettles, J. Cryst. Growth **310**, 887 (2008).
[15] W.-H. Chen, Z.-Y. Qin, X.-Y. Tian, X.-H. Zhong, Z.-H. Sun, B.-K. Li, R.-S. Zheng, Y. Guo, and H.-L. Wu, Molecules **24**, 1562 (2019).
[16] S. Tanaka, R.S. Kern, and R.F. Davis, Appl. Phys. Lett. **66**, 37 (1995).
[17] A. Hickman, R. Chaudhuri, S.J. Bader, K. Nomoto, K. Lee, H.G. Xing, and D. Jena, IEEE Electron Device Lett. **40**, 1293 (2019).
[18] A.G. Baca, A.M. Armstrong, A.A. Allerman, E.A. Douglas, C.A. Sanchez, M.P. King, M.E. Coltrin, T.R. Fortune, and R.J. Kaplar, Appl. Phys. Lett. **109**, 033509 (2016).
[19] H. Tokuda, M. Hatano, N. Yafune, S. Hashimoto, K. Akita, Y. Yamamoto, and M. Kuzuhara, Appl. Phys. Express **3**, 121003 (2010).
[20] N. Yafune, S. Hashimoto, K. Akita, Y. Yamamoto, H. Tokuda, and M. Kuzuhara, Electron. Lett. **50**, 211 (2014).
[21] R. Dargis, A. Clark, A. Ansari, Z. Hao, M. Park, D. Kim, R. Yanka, R. Hammond, M. Debnath, and R. Pelzel, Phys. Status Solidi **217**, 1900813 (2020).
[22] C.-P. Huang, K. Gupta, C.-H. Wang, C.-P. Liu, and K.-Y. Lai, Sci. Rep. **7**, 7135 (2017).
[23] M. Pons, J. Su, M. Chubarov, R. Boichot, F. Mercier, E. Blanquet, G. Giusti, and D. Pique, J. Cryst. Growth **468**, 235 (2017).
[24] M.-A. Dubois and P. Muralt, J. Appl. Phys. **89**, 6389 (2001).
[25] P. Muralt, in edited by H. Bhugra and G. Piazza (Springer International Publishing, Cham, 2017), pp. 3–37.
[26] P. Muralt, R.G. Polcawich, and S. Trolier-McKinstry, MRS Bull. **34**, 658 (2009).
[27] S. Trolier-McKinstry and P. Muralt, J. Electroceramics **12**, 7 (2004).
[28] N. Susilo, S. Hagedorn, D. Jaeger, H. Miyake, U. Zeimer, C. Reich, B. Neuschulz, L. Sulmoni, M. Guttmann, F. Mehnke, C. Kuhn, T. Wernicke, M. Weyers, and M. Kneissl, Appl. Phys. Lett. **112**, 41110

(2018).
[29] Y.R. Koh, Z. Cheng, A. Mamun, M.S. Bin Hoque, Z. Liu, T. Bai, K. Hussain, M.E. Liao, R. Li, J.T. Gaskins, A. Giri, J. Tomko, J.L. Braun, M. Gaevski, E. Lee, L. Yates, M.S. Goorsky, T. Luo, A. Khan, S. Graham, and P.E. Hopkins, ACS Appl. Mater. Interfaces **12**, 29443 (2020).
[30] A. V Inyushkin, A.N. Taldenkov, D.A. Chernodubov, E.N. Mokhov, S.S. Nagalyuk, V.G. Ralchenko, and A.A. Khomich, J. Appl. Phys. **127**, 205109 (2020).
[31] G.A. Slack, R.A. Tanzilli, R.O. Pohl, and J.W. Vandersande, J. Phys. Chem. Solids **48**, 641 (1987).
[32] C. Duquenne, M.-P.P. Besland, P.Y. Tessier, E. Gautron, Y. Scudeller, and D. Averty, J. Phys. D. Appl. Phys. **45**, 15301 (2012).
[33] S. Xiao, R. Suzuki, H. Miyake, S. Harada, and T. Ujihara, J. Cryst. Growth **502**, 41 (2018).
[34] R.L. Xu, M. Muñoz Rojo, S.M. Islam, A. Sood, B. Vareskic, A. Katre, N. Mingo, K.E. Goodson, H.G. Xing, D. Jena, and E. Pop, J. Appl. Phys. **126**, 185105 (2019).
[35] D.G. Cahill, Rev. Sci. Instrum. **75**, 5119 (2004).
[36] J. Zhu, X. Wu, D.M. Lattery, W. Zheng, and X. Wang, Nanoscale Microscale Thermophys. Eng. **21**, 177 (2017).
[37] J. Zhu, H. Park, J.-Y. Chen, X. Gu, H. Zhang, S. Karthikeyan, N. Wendel, S.A. Campbell, M. Dawber, X. Du, M. Li, J.-P. Wang, R. Yang, and X. Wang, Adv. Electron. Mater. **2**, 1600040 (2016).
[38] M.S. Bin Hoque, Y.R. Koh, J.L. Braun, A. Mamun, Z. Liu, K. Huynh, M.E. Liao, K. Hussain, Z. Cheng, E.R. Hoglund, D.H. Olson, J.A. Tomko, K. Aryana, R. Galib, J.T. Gaskins, M.M.M. Elahi, Z.C. Leseman, J.M. Howe, T. Luo, S. Graham, M.S. Goorsky, A. Khan, and P.E. Hopkins, ACS Nano **15**, 9588 (2021).
[39] J.P. Freedman, J.H. Leach, E.A. Preble, Z. Sitar, R.F. Davis, and J.A. Malen, Sci. Rep. **3**, 2963 (2013).
[40] T.E. Beechem, A.E. McDonald, E.J. Fuller, A.A. Talin, C.M. Rost, J.-P. Maria, J.T. Gaskins, P.E. Hopkins, and A.A. Allerman, J. Appl. Phys. **120**, 95104 (2016).
[41] Y. Shen, R. Zhang, R. Vetury, and J. Shealy, in *2020 IEEE Int. Ultrason. Symp.* (2020), pp. 1–3.
[42] R. Liu, F.A. Ponce, A. Dadgar, and A. Krost, Appl. Phys. Lett. **83**, 860 (2003).
[43] O. Ambacher, J. Phys. D. Appl. Phys. **31**, 2653 (1998).
[44] H. Watanabe, N. Yamada, and M. Okaji, Int. J. Thermophys. **25**, 221 (2004).
[45] S. Tamariz, D. Martin, and N. Grandjean, J. Cryst. Growth **476**, 58 (2017).
[46] S. Raghavan and J.M. Redwing, J. Cryst. Growth **261**, 294 (2004).
[47] S.R. Lee, A.M. West, A.A. Allerman, K.E. Waldrip, D.M. Follstaedt, P.P. Provencio, D.D. Koleske, and C.R. Abernathy, Appl. Phys. Lett. **86**, 241904 (2005).
[48] T. Metzger, R. Höpler, E. Born, O. Ambacher, M. Stutzmann, R. Stömmer, M. Schuster, H. Göbel, S. Christiansen, M. Albrecht, and H.P. Strunk, Philos. Mag. A **77**, 1013 (1998).
[49] D. Wang, K. Uesugi, S. Xiao, K. Norimatsu, and H. Miyake, Appl. Phys. Express **13**, 95501 (2020).
[50] J.A. Phys, T.E. Beechem, A.E. Mcdonald, E.J. Fuller, A.A. Talin, C.M. Rost, J.T. Gaskins, P.E. Hopkins, A.A. Allerman, T.E. Beechem, A.E. Mcdonald, E.J. Fuller, A.A. Talin, C.M. Rost, J. Maria, J.T. Gaskins, P.E. Hopkins, and A.A. Allerman, **095104**, (2017).
[51] H. Miyake, C.-H. Lin, K. Tokoro, and K. Hiramatsu, J. Cryst. Growth **456**, 155 (2016).
[52] N. Onojima, J. Suda, T. Kimoto, and H. Matsunami, Appl. Phys. Lett. **83**, 5208 (2003).
[53] R. Rounds, B. Sarkar, A. Klump, C. Hartmann, T. Nagashima, R. Kirste, A. Franke, M. Bickermann, Y. Kumagai, Z. Sitar, and R. Collazo, Appl. Phys. Express **11**, 71001 (2018).
[54] A. Franco Júnior and D.J. Shanafield, Cerâmica **50**, 247 (2004).
[55] P. Bogusławski and J. Bernholc, Phys. Rev. B **56**, 9496 (1997).
[56] J. Zou, D. Kotchetkov, A.A. Balandin, D.I. Florescu, and F.H. Pollak, J. Appl. Phys. **92**, 2534 (2002).
[57] M. Akiyama, T. Kamohara, K. Kano, A. Teshigahara, and N. Kawahara, Appl. Phys. Lett. **93**, 21903 (2008).
[58] G.A. Slack, L.J. Schowalter, D. Morelli, and J.A. Freitas, J. Cryst. Growth **246**, 287 (2002).
[59] M.A. Signore, A. Taurino, D. Valerini, A. Rizzo, I. Farella, M. Catalano, F. Quaranta, and P. Siciliano,

J. Alloys Compd. **649**, 1267 (2015).
[60] J.W. Lee, J.J. Cuomo, Y.S. Cho, and R.L. Keusseyan, J. Am. Ceram. Soc. **88**, 1977 (2005).
[61] S. Fleischmann, E. Richter, A. Mogilatenko, M. Weyers, and B. Sapphire, J. Cryst. Growth **507**, 295 (2019).
[62] D. Fu, Q. Wang, G. Zhang, R. Zhu, H. Liu, Z. Li, and L. Wu, J. Cryst. Growth **551**, 125902 (2020).
[63] Y.-C. Yang, C.-T. Chang, Y.-C. Hsiao, J.-W. Lee, and B.-S. Lou, Surf. Coatings Technol. **259**, 219 (2014).
[64] C.H. Park, J.G. Kim, S.-G. Jung, D.J. Lee, Y.W. Park, and B.-K. Ju, Sci. Rep. **9**, 8690 (2019).
[65] F.Y.C. Boey, X.L. Song, Z.Y. Gu, and A. Tok, J. Mater. Process. Technol. **89**–**90**, 478 (1999).
[66] C.T. Warner, T.M. Hartnett, D. Fisher, and W. Sunne, in *Proc.SPIE* (2005).
[67] Y. Zheng, M. Park, A. Ansari, C. Yuan, and S. Graham, in *2021 21st Int. Conf. Solid-State Sensors, Actuators Microsystems* (2021), pp. 321–324.
[68] J. Wang, Y. Zheng, and A. Ansari, Phys. Status Solidi – Rapid Res. Lett. **15**, 2100034 (2021).
[69] S.S. Iyer and R.N. Candler, Phys. Rev. Appl. **5**, 34002 (2016).
[70] Y. Song, C. Perez, G. Esteves, J.S. Lundh, C.B. Saltonstall, T.E. Beechem, J.I. Yang, K. Ferri, J.E. Brown, Z. Tang, J.-P. Maria, D.W. Snyder, R.H. Olsson, B.A. Griffin, S.E. Trolier-McKinstry, B.M. Foley, and S. Choi, ACS Appl. Mater. Interfaces (2021).
[71] K. Uesugi, Y. Hayashi, K. Shojiki, and H. Miyake, Appl. Phys. Express **12**, 65501 (2019).
[72] Z. Hao, M. Park, D.G. Kim, A. Clark, R. Dargis, H. Zhu, A. Ansari, and N.A. Nw, 2019 IEEE MTT-S Int. Microw. Symp. 786 (2019).
[73] W. Zhou, R. Apkarian, Z.L. Wang, and D. Joy, in edited by W. Zhou and Z.L. Wang (Springer New York, New York, NY, 2007), pp. 1–40.
[74] J.S. Lundh, K. Coleman, Y. Song, B.A. Griffin, G. Esteves, E.A. Douglas, A. Edstrand, S.C. Badescu, E.A. Moore, J.H. Leach, B. Moody, S. Trolier-McKinstry, and S. Choi, J. Appl. Phys. **130**, 44501 (2021).
[75] Y. Wang, J.Y. Park, Y.K. Koh, and D.G. Cahill, J. Appl. Phys. **108**, 43507 (2010).
[76] J. Zhu, H. Park, J.-Y. Chen, X. Gu, H. Zhang, S. Karthikeyan, N. Wendel, S.A. Campbell, M. Dawber, X. Du, M. Li, J.-P. Wang, R. Yang, and X. Wang, Adv. Electron. Mater. **2**, (2016).
[77] J. Zhu, T. Feng, S. Mills, P. Wang, X. Wu, L. Zhang, S.T. Pantelides, X. Du, and X. Wang, ACS Appl. Mater. Interfaces **10**, 40740 (2018).
[78] T. Feng, X. Wu, X. Yang, P. Wang, L. Zhang, X. Du, X. Wang, and S.T. Pantelides, Adv. Funct. Mater. **30**, 1907286 (2020).
[79] A.J. Schmidt, R. Cheaito, and M. Chiesa, Rev. Sci. Instrum. **80**, 94901 (2009).
[80] J.L. Braun, D.H. Olson, J.T. Gaskins, P.E. Hopkins, D.H. Olson, and J.T. Gaskins, Rev. Sci. Instrum. **90**, 24905 (2019).
[81] Y. Song, D. Shoemaker, J.H. Leach, C. McGray, H.-L. Huang, A. Bhattacharyya, Y. Zhang, C.U. Gonzalez-Valle, T. Hess, S. Zhukovsky, K. Ferri, R.M. Lavelle, C. Perez, D.W. Snyder, J.-P. Maria, B. Ramos-Alvarado, X. Wang, S. Krishnamoorthy, J. Hwang, B.M. Foley, and S. Choi, ACS Appl. Mater. Interfaces **13**, 40817 (2021).
[82] C.A. Ratsifaritana and P.G. Klemens, Int. J. Thermophys. **8**, 737 (1987).

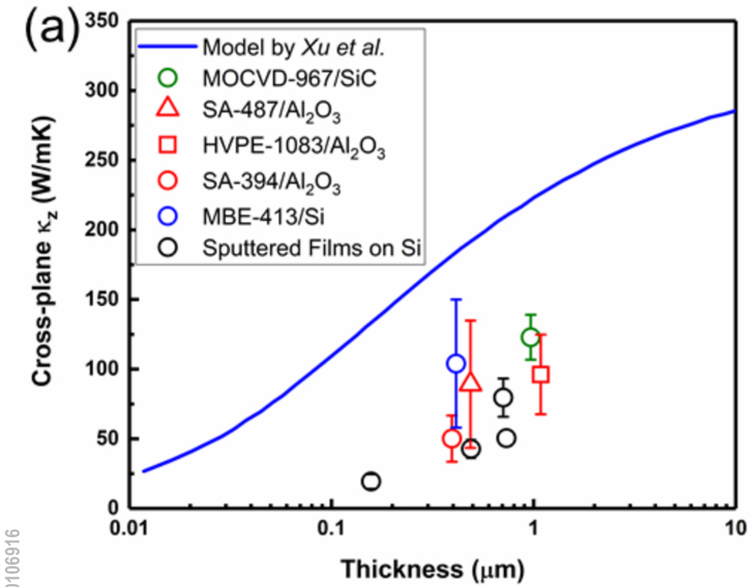

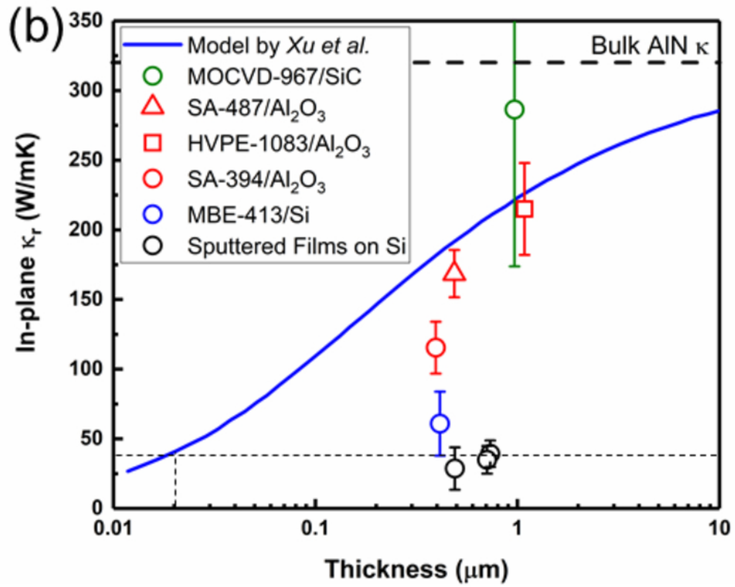

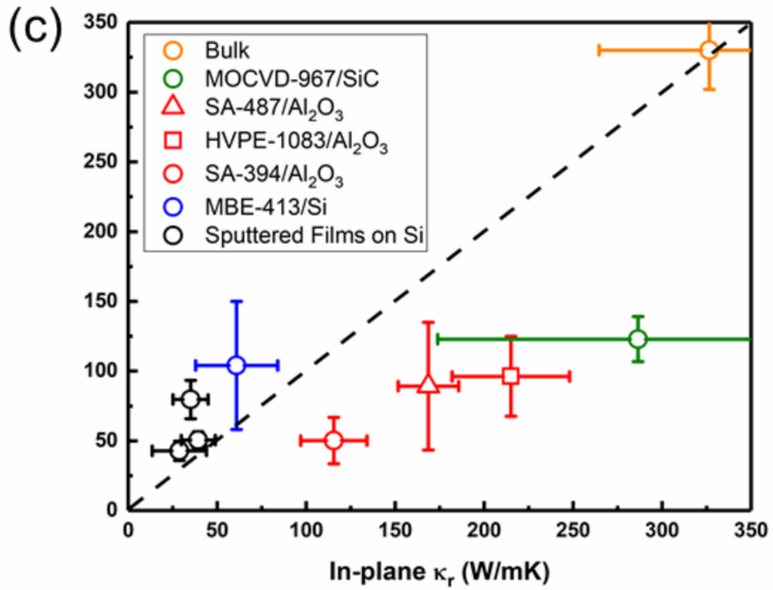

Journal of Applied Physics
AIP Publishing

Journal of Applied Physics

AIP Publishing

Journal of Applied Physics

Journal of Applied Physics

Journal of Applied Physics

AIP Publishing

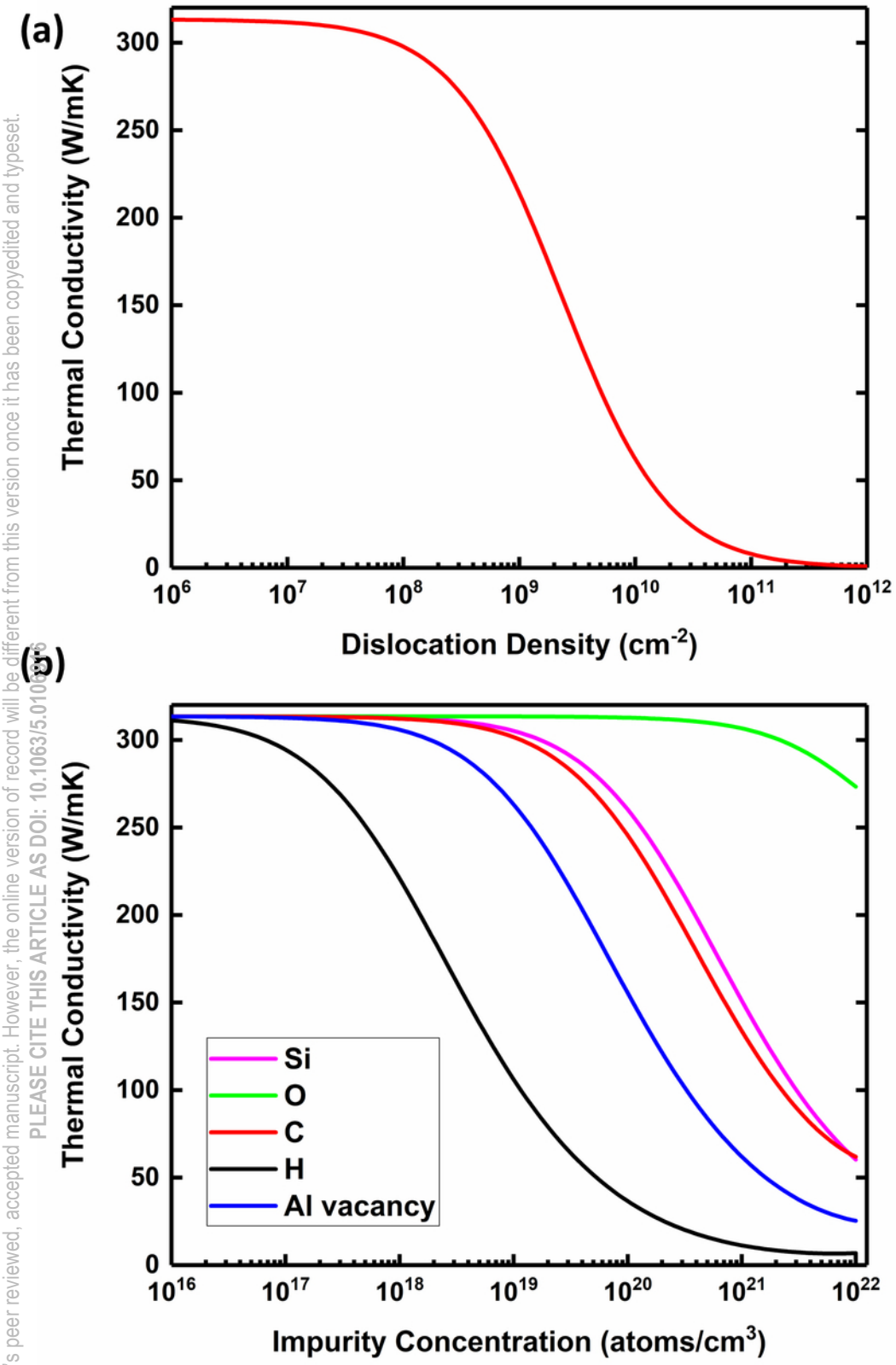

Journal of Applied Physics

AIP Publishing

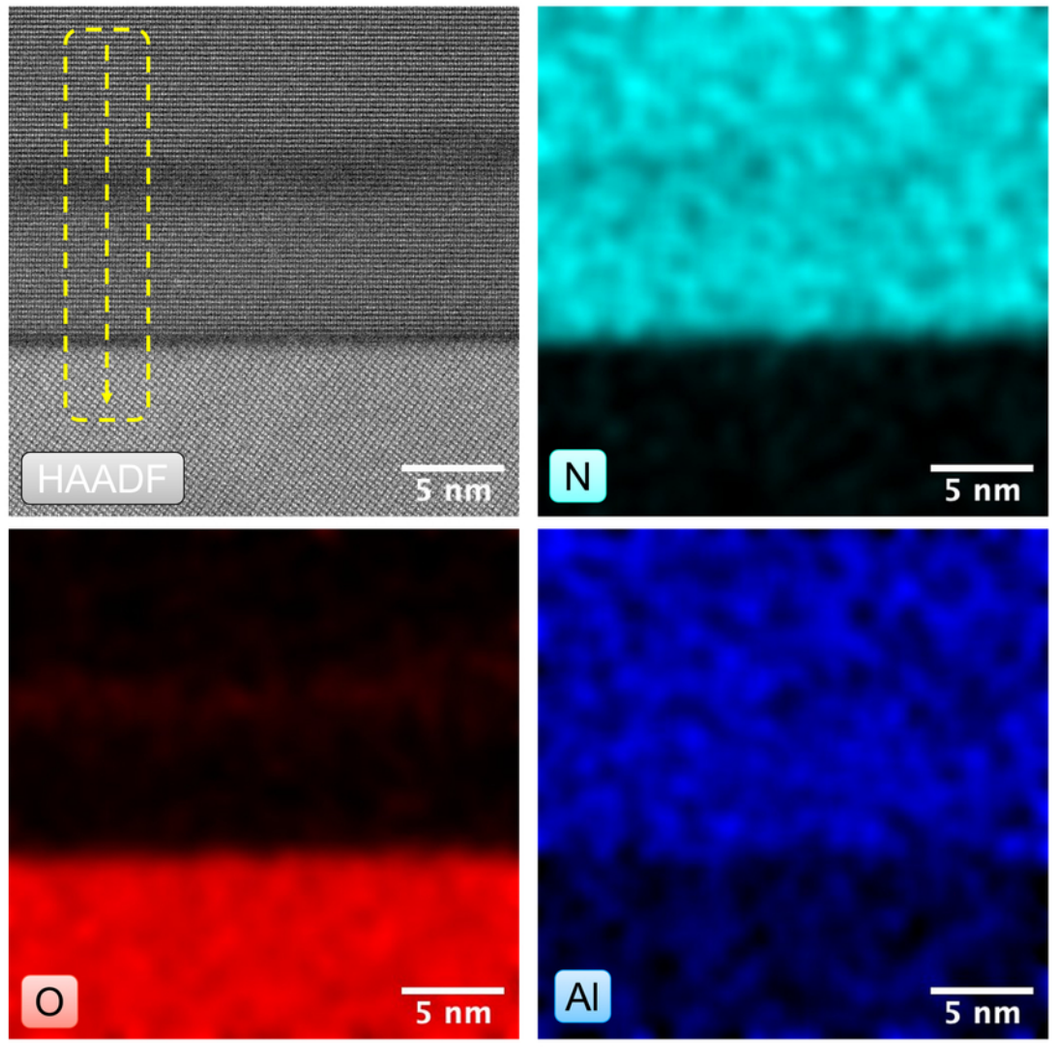

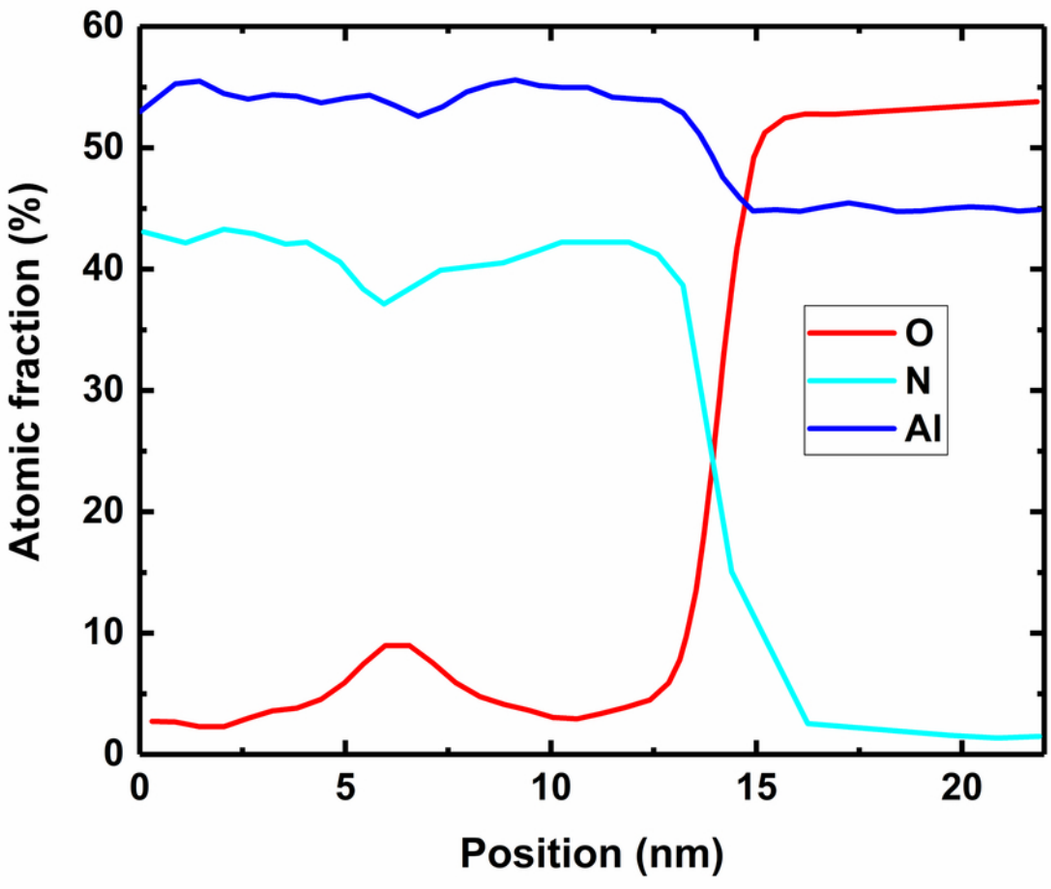

Journal of Applied Physics

AIP Publishing

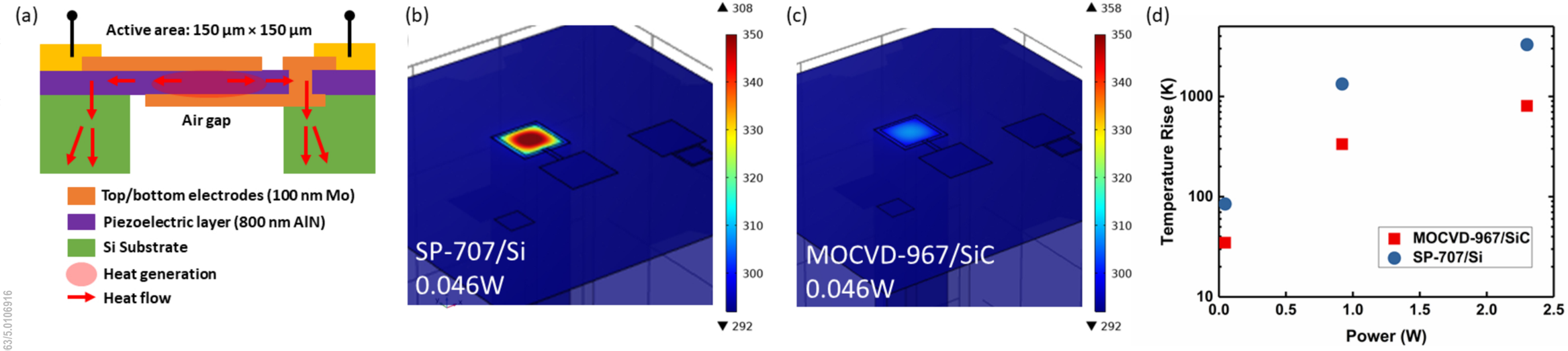

Journal of Applied Physics

AIP Publishing